Radiation-induced Attenuation in Standard Optical Fibers at Cryogenic Temperatures: Dose Rate, Temperature, and Photobleaching Interdependence

Fernando S. Fernandez, Joseph J. Schuyt, Shahna M. Haneef, Dominic A. Moseley, *Member*, *IEEE*, Bartholomew M. Ludbrook, *Member*, *IEEE*, Rodney A. Badcock, *Fellow*, *IEEE*

***Abstract*—The use of optical fiber sensors in ionizing radiation environments is complicated by radiation-induced attenuations (RIAs) that cause significant signal loss as the cumulative radiation dose increases. Moreover, the RIA growth kinetics are strongly dependent on the temperature of irradiation and the wavelengths and intensities of the probe and/or photobleaching lights. Herein, we experimentally investigated the interdependence of the high-dose RIA, radiation dose rate (up to 8.7 Gy s^{-1}), irradiation temperature (down to 15 K), and photobleaching power, in standard germanosilicate optical fibers (SMF28e+). Generally, the RIA increased as a function of dose rate and decreased as functions of temperature and photobleaching power. The experimental high-dose (i.e., saturation) RIA data were fit to a simple kinetic model with quantitative accuracy. Thus, we validate the model, demonstrating that the model accurately captures the interdependence of three key experimental parameters. Using a single set of fiber-specific constants, the saturation RIA was accurately calculated over a broad range of dose rates, temperatures, and photobleaching powers, and across distinct experiments.**

***Index Terms*—Cryogenic, irradiation, optical fiber, photobleaching, radiation-induced attenuation.**

I. INTRODUCTION

OPTICAL fiber sensors (OFS) are immune to electromagnetic interference, can operate over wide temperature ranges, and, in some circumstances, can survive significant doses of ionizing radiations [1]. Consequently, modern research has focused on testing OFS under the "extreme" conditions encountered in space [2], [3], nuclear fusion facilities [4], [5], high-energy physics laboratories [6], [7], and various other harsh or volatile environments [8], [9], [10]. While OFS have been successfully implemented in several cases, their functionalities are often limited by the environment. The severity of these limitations depends on the type of OFS (i.e., the nature of the sensing element), the type of fiber (i.e., the chemical composition of the fiber), and the configuration of the optical network. Toward the development of new sensors, it is necessary to understand the mechanisms through which sensing may be limited, and to develop techniques through which these limitations may be suppressed. To that end, it is important to understand the interdependence of convoluted environmental effects.

Ionizing radiations produce numerous absorptive defects in optical fibers, which manifest radiation induced attenuations (RIA) spanning a massive range of wavelengths (ultraviolet through visible through infrared) [11]. As RIA can cause significant signal losses in both active sensing and the generic transmitting optical fiber elements, exposure to ionizing radiations limits the functionality of OFS. If the RIA exceeds some threshold, any signal corresponding to the measurand, or other data, will be indistinguishable from noise. Then, the lifetime of any such system is effectively determined by how rapidly this threshold RIA is reached. When the radiation dose rate is sufficiently small (e.g., space), the fiber system may survive for years. Conversely, when the radiation dose rate is very large (e.g., fusion), the system lifetime may be very short.

The severity of RIA strongly depends on both the fiber composition and the temperature at which the irradiation occurs [12-20]. The irradiation temperature may affect both the generation and recombination rates of radiation-induced defects [R5]. When the ratio of recombination/generation increases, RIA is reduced, and vice versa. In some cases, thermal effects lag radiation effects, manifesting complicated RIA kinetics [R5]. Generally, the high-dose (long-time) RIA at which the thermal and radiation effects equilibrate is larger at low temperatures, though this is not always the case (e.g., P-doped fibers) [20]. For example, radiation-tolerant fibers (F-doped) exhibit RIA (measured near 1550 nm) of several 1 dB/km after exposure to a gamma dose of approximately 10 kGy, at room temperature [18]. Standard (Ge-doped) fibers exhibit much larger RIA (over 100 dB/km) under the same experimental conditions [19]. If these same fibers are instead irradiated at very low temperatures (e.g., 16 K), the RIA of the F-doped fiber increases to several 100 dB/km, and the RIA of the Ge-doped fiber increases to over 10000 dB/km [18], [19]. Thus, high-dose RIA may vary by several orders of magnitude depending on the fiber composition and irradiation temperature. Generally, the RIA is larger at low temperatures, though this is not always the case (e.g., P-doped fibers) [20].

This work was supported by the New Zealand Ministry of Business, Innovation, and Employment (MBIE) Catalyst Fund under RTVU1916. FSF acknowledges support from the Dodd-Walls Center Output Award. We thank Bill Trompetter (GNS) for assistance with radiation safety and operation.

F.S.F. and J.J.S. contributed equally to this work. *Corresponding author: Joseph J. Schuyt. Email: joe.schuyt@vuw.ac.nz*.

The authors are with the Paihau–Robinson Research Institute, Victoria University of Wellington, Lower Hutt 5046, New Zealand. F.S.F., J.J.S., S.M.H., B.M.L., and R.A.B., are also with Te Whai Ao – Dodd-Walls Center for Photonic and Quantum Technologies, Lower Hutt 5046, New Zealand. R.A.B., is also with OpenStar Technologies, Wellington 6035, New Zealand.

Color versions of one or more of the figures in this article are available online at http://ieeexplore.ieee.org

The fact that even radiation-tolerant fibers suffer large RIA at cryogenic temperatures complicates the use of OFS in cryogenic radiation-rich environments, e.g., HTS magnets in fusion facilities. Alongside chemical hardening techniques, RIA can be further suppressed via *photobleaching*. Photobleaching, also known as optical annealing, occurs when radiation-induced defects are bleached via exposure to light [21–26]. The photobleaching light may be the same as the OFS probe light (primary photobleaching), or light of a different wavelength (secondary photobleaching). The overall effectiveness of photobleaching depends on the wavelength and power of the photobleaching light, relative to the absorption profile of the defect(s) that manifest the RIA [24]. Several recent works have demonstrated that photobleaching can be used to suppress RIA in different fibers by over an order of magnitude [24], [25], [26]. Consequently, future OFS are likely to employ photobleaching as an RIA suppression technique, complementing traditional chemical hardening techniques.

The radiation dose rate, the temperature of irradiation, and the intensity of the photobleaching light will all play a major role in determining the RIA behavior of any OFS. The dose rate will determine the rate at which defects are generated, the temperature will determine which defects are generated and at what rate, and/or which defects are thermally annealed and at what rate, and the intensity of the photobleaching light will determine which defects are optically annealed and at what rate. In the high-dose limit (i.e., large cumulative doses, generally at least 10 kGy), the magnitude of the RIA will likely depend on some equilibrium conditions wherein the defect generation and recombination rates, determined by the input parameters, balance. A recent model attempted to analytically relate this equilibrium RIA to the input parameters with some success [27]. Should such a model prove viable, it will enable one to predict the high dose RIA of OFS in different environments. Thus, one could, for example, determine whether the RIA would prevent the implementation of OFS, or how much photobleaching light would be required to keep RIA below some threshold. This will be particularly useful in a fusion context, as experimental testing under fusion conditions is difficult at present.

Germanosilicate fibers exhibit numerous radiation-induced defects related to both the silica network and the Ge dopant [R2]. Spectrally-resolved RIA measurements have enabled the identification of distinct defects that dominate the RIA at different wavelengths under different experimental conditions (e.g., temperatures and cumulative doses). A recent work [24] established that the RIA at 1550 nm, at low temperatures (-100°C is predominantly caused by GeY centers, with additional contributions by GeX centers and different types of self-trapped holes (STHs). The RIA at shorter wavelengths (e.g., 1050 nm), also at low temperatures, is dominated by th same defects with different relative weights [24]. Furthermore, photobleaching with wavelengths <1550 nm was shown to effectively reduce the concentrations of the GeX and GeY centers at low temperatures, while the effect of photobleaching on Ge-related STHs was insignificant [24]. Consequently, it is of interest to investigate the efficacy of short-wavelength photobleaching at even lower temperatures, at which the

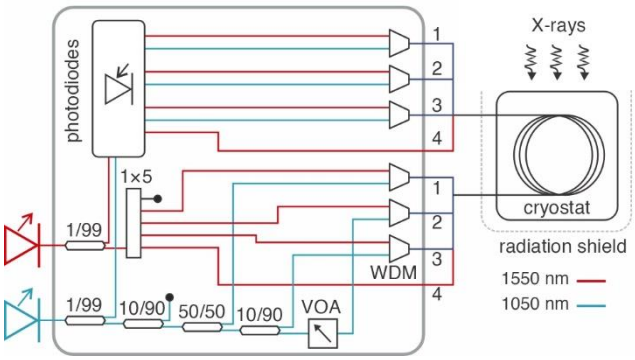

Fig. 1. Schematic of the experimental setup. X/Y and X×Y = fiber splitters, VOA = variable optical attenuator, WDM = wavelength division multiplexer.

nature of the defects may be similar or distinct to those observed at -100°C.

The purpose of this work was two-fold. First, we experimentally characterized the RIA of a commonly employed germanosilicate optical fiber (Corning SMF28e+) under different experimental conditions to investigate the interdependence of the radiation dose rate, photobleaching rate, and temperature. Second, we tested the ability of a model [27] to quantitatively describe the experimental results, and to predict the RIA under different conditions using a single set of parameters characteristic of the fiber-type. We present the results of experiments in which the RIA at 1550 nm of Corning SMF28e+ fibers was measured as a function of radiation dose rate, radiation temperature, and photobleaching power (at 1050 nm). The 1050 nm photobleaching wavelength was selected as it is known to effectively reduce RIA at 15 K [21], [22], and so our results could be compared to those presented in earlier works.

Fibers were exposed to large cumulative doses (>1 MGy) over a wide temperature range (15 K – 200 K). Saturated RIA values, corresponding to defect generation/recombination equilibria, were observed under different conditions. The data were successfully quantitatively interpreted using the kinetic model.

II. Experimental

Optical fibers were irradiated with steady-state X-rays using a custom-built irradiation setup in the Cryogenic Irradiation of Superconductors and Optical Fibres Laboratory (CRISOL) at Paihau-Robinson Research Institute, NZ. The X-ray source is a Comet MXR 321 (W target) with an operating voltage of 320 kV, integrated with a custom-built cryostat with 8 fiber feedthroughs. Fiber samples were wound about a copper bobbin that was attached to the cryostat coldhead (CryoPride KDE210SA). A small amount of Apiezon N vacuum grease was applied to each layer of fibers to prevent pinching and micro-bending, and to ensure good thermal contact (i.e., a uniform temperature distribution across the fibers). The aluminum exterior of the cryostat between the mounted fibers and the X-ray source is only 0.5 mm thick to minimize attenuation. The temperature of the copper is monitored via an attached Cernox thermometer, and the

temperature is controlled via a Lakeshore 35 temperature controller. In this configuration, the absorbed dose rate to standard Ge-doped fibers at the maximum operating current (10 mA) is calculated as 8.7 Gy s^{-1}. A detailed explanation of these calculations is given in [22]. Briefly, the X-ray spectrum seen by the fibers was simulated using the parameters of the X-ray source and the precise geometry of the experimental apparatus, accounting for cryostat attenuation. Subsequently, the absorbed dose to Ge-doped silica was calculated using the energy-dependent mass-energy absorption coefficients.

The Corning SMF28e+ fibers are germanosilicate fibers (Ge concentration ~4 wt% [R4]) with a cutoff wavelength at 1260 nm. Consequently, the fibers are single mode at the probe wavelength (1550 nm) and multi-modal at the photobleaching wavelength (1050 nm).

Two distinct experiments were performed in this work. For the first experiment, the X-ray dose rate was controlled via the operating current of the X-ray source (from 2 mA to 10 mA) while the sample temperature was kept constant at 15 K. For the second experiment, the X-ray dose rate was kept constant at the maximum operating current, while the sample temperature was decreased from 200 K to 15 K. For both experiments, the optical configuration shown in Fig. 1 was utilized. The number of available cryostat feedthroughs limited the number of fibers per experiment to 4 total (per the 4 input/output pairs). All tested fibers were from a single batch of Corning SMF-28e+ standard fiber cut to a length of 2 m + up to 0.2 m for splicing. New fibers were used for each experiment. The transmission of 1550 nm light supplied by a Thorlabs S5FC1005S superluminescent diode (SLD) through each fiber was continuously monitored throughout each experiment, and the measured output prior to irradiation was approximately equivalent across all fibers and both experiments (~2 mW) (Table I). Part (1%) of the 1550 nm output was monitored via a non-irradiated length of fiber that functioned as a reference signal. Photobleaching light at 1050 nm supplied by a Thorlabs SLD1050S SLD (8 mW) was additionally coupled into 3 of the 4 fibers via a series of couplers and wavelength division multiplexers (WDMs). Again, 1% of the 1050 nm output was monitored via non-irradiated fiber as a reference. The 1050 nm couplers and an associated variable optical attenuator were configured such that different powers were delivered to each fiber, ranging from 0 mW to approximately 4 mW (Table I). After transmission via irradiated fiber, the 1050 nm and 1550 nm signals were separated via WDMs and directed to FC/APC coupled photodiodes (Thorlabs FGA01FC) connected to transimpedance amplifiers. The measured outputs were read via NI-9205 card, and the experiment was controlled via LabView software. Each datapoint corresponds to an average of 20 measurements taken over 10 s. All optical components were installed in a temperature-controlled box to reduce thermal fluctuations.

Prior to each experiment, the optical powers at 1550 nm (P_{1550}) and 1050 nm (P_{1050}) in each fiber were measured at the input of the vacuum fiber feedthrough (Table I).

TABLE I

PROBE AND PHOTOBLEACHING OPTICAL POWERS

	Experiment 1: Dose Rate Influence (15 K)				Experiment 2: Temperature Influence (8.7 Gy s^{-1})			
Fiber	1	2	3	4	1	2	3	4
P_{1550} (mW)	1.97	1.75	1.37	2.55	2.18	1.43	1.83	2.55
P_{1050} (mW)	4.01	0.84	0.10	0	3.62	0.66	0.093	0

III. RESULTS

The results of Experiment 1 are shown in Fig. 2. As a primary goal of the experiment was to obtain representative saturation RIA values, i.e., $RIA_{sat}(\Phi, \varphi, T)$ (Φ = X-ray dose rate, φ = photobleaching rate, T = temperature) values, the total time for which each fiber was exposed to each dose rate was varied, such that the $RIA(D)$ (for cumulative dose D) values approached equilibria for most dose rates. The experiment was composed of 10 distinct steps, the first corresponding to the initial ramp of the X-ray source current, and the subsequent steps corresponding to distinct dose rates from 1.74 Gy s^{-1} (2 mA) to 8.7 Gy s^{-1} (10 mA). We denote the RIA at the end of each step as RIA_{end}. At the lowest dose rate (1.74 Gy s^{-1}), $RIA(D)$ was increasing rapidly even after 24 hours of continuous irradiation (150 kGy), such that RIA_{end} will be an underestimation of RIA_{sat}. In an earlier work [22], we established that a 150 kGy dose was sufficient to approximately saturate the RIA at 15 K at the highest dose rate employed in this work (8.7 Gy s^{-1}). Thus, the cumulative dose at which saturation occurs depends strongly on the dose rate, even at 15 K.

The growth of $RIA(D)$ toward the end of each following irradiation period (i.e., all higher dose rates) was small, such that RIA_{end} is taken as a good approximation of RIA_{sat}. The total period of irradiation for Experiment 1 was approximately 90 hours and the total cumulative dose was approximately 1.5 MGy.

The data in Figs 2a–2e demonstrate that: (1) increasing the radiation dose rate increases the cumulative ($RIA(D)$) and equilibrium (RIA_{sat}) RIA values; (2) successive dose rate increases result in successively smaller increases in the RIA saturation values; and (3) the cumulative and equilibrium RIA values are smaller for larger 1050 nm photobleaching powers at all dose rates.

Result (1) is interpreted as follows: as the dose rate increases, the defect generation rate increases; as the temperature and photobleaching powers are kept constant, the total defect bleaching rate remains constant. Therefore, the generation/bleaching ratio increases, and the RIA equilibrium values concomitantly increase. Result (3) is expected as 1050 nm light is known to effectively bleach defects that contribute to RIA at 1550 nm over a wide temperature range [21], [22]. Here, the maximum RIA in the fiber with no 1050 nm photobleaching light was approximately 6000 dB/km, and the maximum RIA in the fiber with 4 mW 1050 nm

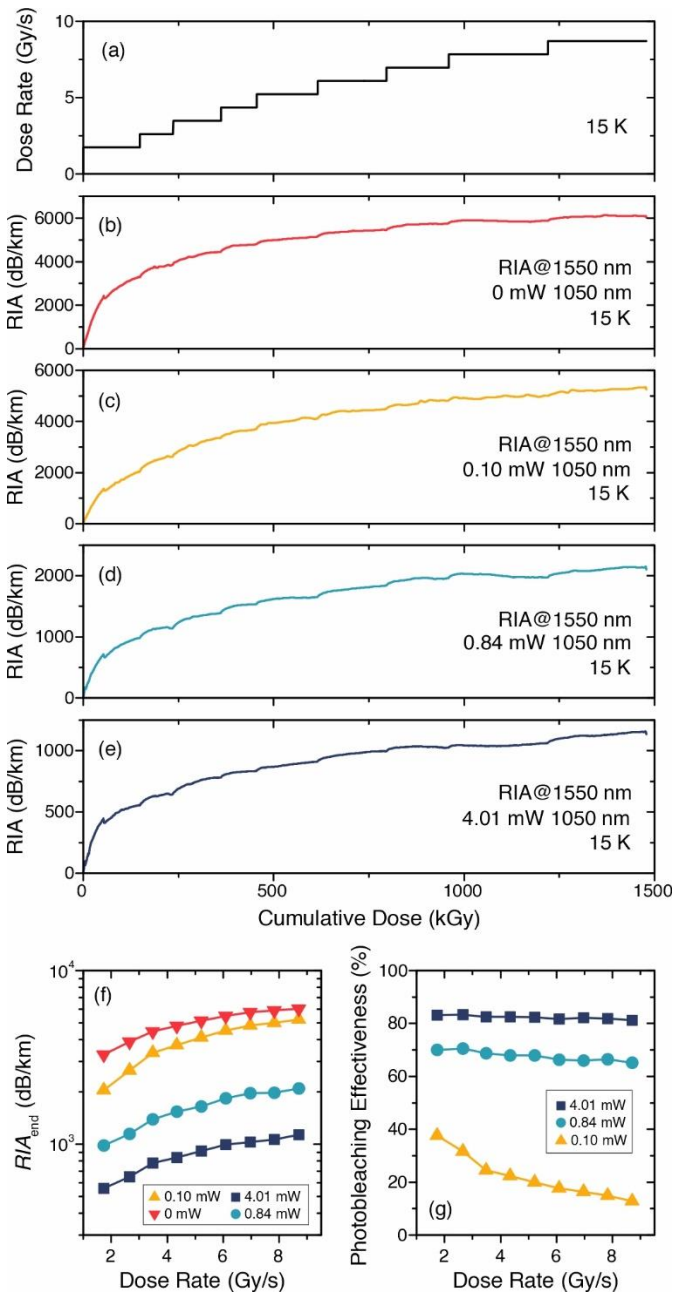

Fig. 2. (a) Calculated dose rate to the fibers as a function of the cumulative dose received by the fibers. (b)—(e) Measured RIA at 1550 nm in each fiber as a function of the cumulative dose received by the fiber, where each fiber was stimulated with different powers of photobleaching light: (b) 0 mW; (c) 0.10 mW; (d) 0.84 mW; (e) 4.01 mW. All fibers were irradiated at 15 K. (f) Final RIA value of each irradiation step (RIA_{end}) versus the dose rate during that same step. (g) Photobleaching effectiveness for each 1050 nm power versus the dose rate.

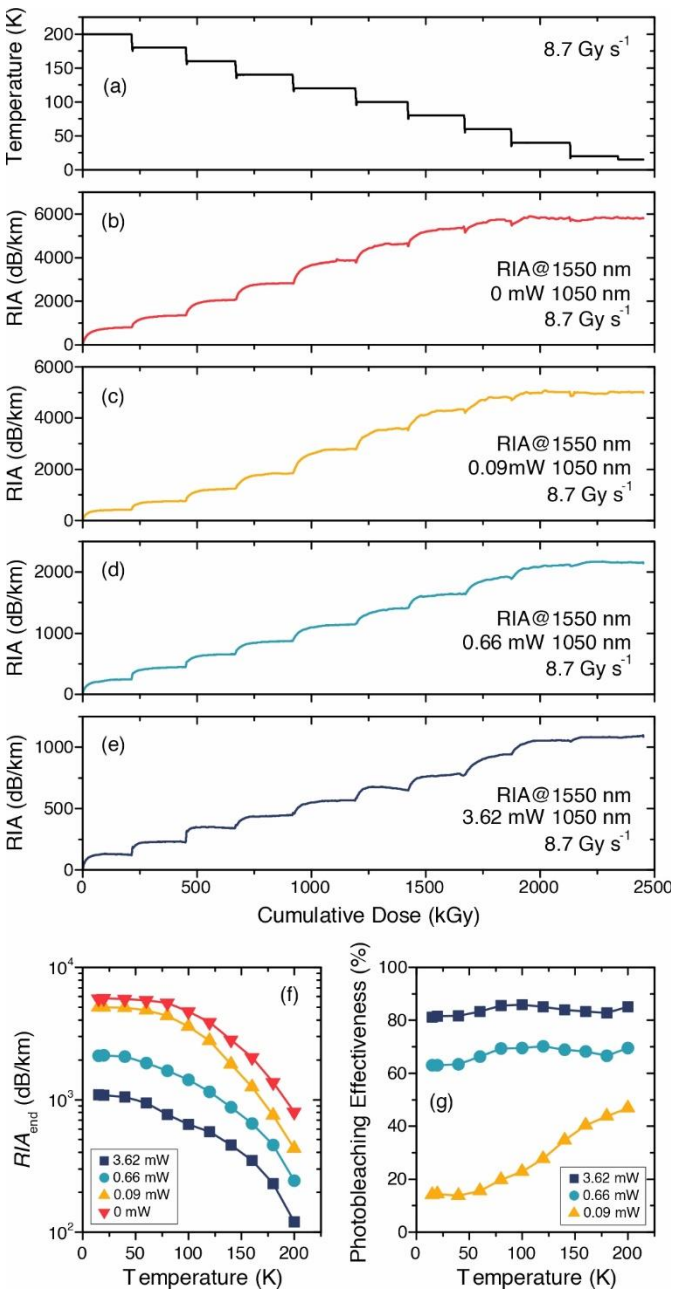

Fig. 3. (a) The measured temperature of the fibers as a function of the cumulative dose received by the fibers. (b)—(e) Measured RIA at 1550 nm in each fiber as a function of the cumulative dose received by the fiber, where each fiber was stimulated with different powers of photobleaching light: (b) 0 mW; (c) 0.09 mW; (d) 0.66 mW; (e) 3.62 mW. All fibers were irradiated at 8.7 Gy s^{-1}. (f) Final RIA value of each irradiation step (RIA_{end}) versus the temperature during that same step. (g) Photobleaching effectiveness for each 1050 nm power versus the temperature.

photobleaching light was approximately 1000 dB/km. Result (2) is less intuitive. One might expect RIA_{end} to increase proportionally to the generation/bleaching ratio, which increases by a factor of 5 (10 mA/2 mA) over the course of the experiment, though this is not the case. In fact, RIA_{end} tends toward a saturated value as the dose rate increases (Fig. 2f). The result suggests that there is an intrinsic equilibrium RIA even in the absence of bleaching, in accordance with standard dynamic models [27], [28]. This will be discussed in detail in Section IV.

We also considered the effect of dose rate on the 1050 nm photobleaching effectiveness (η_{PB}), defined as:

$$\eta_{\mathrm{PB}} = 1 - \frac{RIA_{\max}(P_{1050})}{RIA_{\max}(0)}. \qquad (1)$$

In this case, we let $RIA_{\max}(\Phi) = RIA_{\mathrm{end}}(\Phi)$ for each irradiation step. The photobleaching effectiveness was much greater for higher photobleaching powers, though decreased as the dose rate increased for all 1050 nm powers (Fig. 2g). Further, the decrease in effectiveness with increasing dose rate was smaller for higher photobleaching powers. Again, these results were expected as the defect generation/bleaching ratio increases with dose rate.

The results of Experiment 2 are shown in Fig. 3. Again, the goal was to obtain representative $RIA_{\mathrm{sat}}(\Phi, \varphi, T)$ values. The experiment was composed of 11 distinct steps, during which the fibers were irradiated with a high constant dose rate (8.7 Gy s^{-1}), and where each step corresponded to a different sample temperature ranging from 200 K to 15 K. Again, we denote the RIA at the end of each step as RIA_{end}. As the dose rate was large and constant and the temperature was swept from high to low, equilibria were rapidly reached, compared to Experiment 1. Thus, samples were held at each temperature for similar times. The total period of irradiation for Experiment 2 was approximately 79 hours and the total cumulative dose was approximately 2.5 MGy.

The RIA data in Fig. 3 were calculated relative to the pre-irradiation transmission values at 200 K. Thus, the calculated RIA values also incorporate any temperature-induced transmission changes not related to radiation induced defects (e.g., refractive index changes) that occur during cooling from 200 K to 15 K. Herein, it is assumed that the attenuation unrelated to radiation is small, relative to the actual RIA, and we make no attempt to correct for the former. This assumption will certainly hold for the fibers with low photobleaching powers (large RIA), though the relative influence of non-radiation effects will increase for higher photobleaching powers, as the total RIA reduces.

The data in Figs 3a–3e demonstrate that: (1) decreasing the temperature of irradiation increases the cumulative and equilibrium RIA values; (2) the largest relative changes in the RIA occur for temperatures approximately midway through the temperature sweep, i.e., the changes were smallest at high temperatures (near 200 K) and low temperatures (near 15 K); and (3) the cumulative and equilibrium RIA values are smaller for higher 1050 nm photobleaching powers at all temperatures.

Result (1) is interpreted as follows: as the temperature decreases, the defect bleaching rate decreases (thermal annealing is reduced); as the dose rate is kept constant, the defect generation rate remains constant. Therefore, the generation/bleaching ratios increase, and the RIA equilibrium values concomitantly increase. Result (3) is expected as before, where the data demonstrate that 1050 nm light effectively photobleaches RIA relevant defects over the entire temperature range 15 K – 200 K. Result (2) suggests that distinct defects drive the RIA at 200 K and at 15 K, where there is a transition between defect dominance between these temperatures as the low-temperature defects stabilize (Figs 3f, 3g). RIA_{end} only increased slightly at temperatures below approximately 60 K, suggesting the responsible defect is stabilized at these temperatures. This is in accordance with existing data and dynamic models [24], [27], [29]. This will be discussed in detail in Section IV.

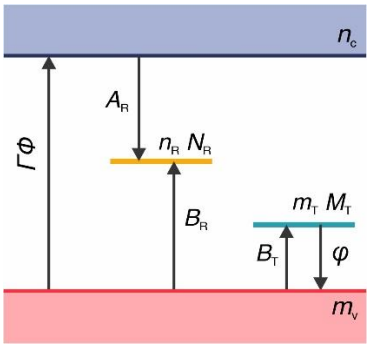

Fig. 4. Schematic of the one trap one recombination center model used to derive the saturation RIA expressions (adapted from [27]). For the meanings of each parameter see the text.

We also considered the effect of dose rate on the 1050 nm photobleaching effectiveness (η_{PB}) (1) (Fig. 3g). We let $RIA_{\max}(\Phi) = RIA_{\mathrm{end}}(\Phi)$ for each irradiation step. The average photobleaching effectiveness was larger for higher photobleaching powers. For small P_{1050} = 0.09 mW, the photobleaching effectiveness increased as a function of temperature, through an apparent transition from 100 K – 150 K. The effectiveness then increased from 14% at 15 K to 47% at 200 K. For larger P_{1050} = 0.66 mW and 3.62 mW, different behavior was observed. The photobleaching effectiveness increased from 15 K to a peak near 100 K, then decreased again up to 180 K, before increasing again. The highest temperature (200 K) η_{PB} values were slightly larger than those at the lowest temperature (15 K): η_{PB}(3.62 mW, 15 K) = 81%, η_{PB}(3.62 mW, 200 K) = 85%, and η_{PB}(0.66 mW, 15 K) = 63%, η_{PB}(3.62 mW, 200 K) = 69%. In all datasets a transition was observed between the two temperature extremes, though the behavior for low and high photobleaching powers was discordant.

IV. Discussion

In a recent article [27], we developed a kinetic model through which equations connecting the saturation RIA during active photo- or thermal- bleaching (RIA_{sat}), the zero-bleaching saturation RIA (RIA_{T}), the thermal- (φ_{q}) and photo- (φ_{P}) bleaching rates, and the radiation dose rate (Φ) were derived. When tested against the limited number of available datasets for which RIA_{sat} versus φ_{q}, φ_{P}, and/or Φ data were available, the expressions proved viable, accurately predicting RIA_{sat} values under different experimental conditions. Importantly, the model is agnostic as to the nature of the individual defect(s) that causes the RIA. To the best of our knowledge, the precise origin of the RIA in germanosilicate fibers at very low temperatures (i.e., 15 K) is unknown. It may relate to the aforementioned GeX, GeY, and Ge-STH defects that dominate the RIA at higher temperatures [24], or some alternative defect(s) that stabilizes at low temperatures. Regardless, the experiments presented in this work were designed to test this model more extensively, such that the

strengths and weaknesses (i.e., limitations) of the model could be determined.

Expressions were derived from a one trap one recombination center (OTOR) kinetic system (Fig. 4) composed of a single electron trap (R) that doubled as a recombination center and a single hole trap (T) with an absorption profile that produced the RIA. Concentrations of electrons in the conduction band (n_C) and holes in the valence band (m_V) are generated at a rate proportional to the dose rate multiplied by the concentration of electron-hole pairs generated per unit dose ($\Gamma\Phi$). The probability for which conduction band electrons are captured by R centers is denoted A_R and the probability for which valence band holes are captured by T centers is denoted B_T. The electron-hole recombination probability at R centers is denoted B_R. The model presumes a finite concentration of pre-existing R and T centers that can trap electrons and holes, respectively, given by N_R and M_T, respectively. The instantaneous concentrations of electrons trapped at R centers and holes trapped at T centers are denoted n_R and m_T, respectively. Finally, the rate at which holes are excited from T centers to the valence band, i.e., the bleach rate of the RIA-active defect, is denoted φ.

Ultimately, the following expression was derived:

$$RIA_{\mathrm{sat}} = 2RIA_{\mathrm{T}} \Big/ \left(1 + \sqrt{1 + 2\omega\frac{\varphi}{\Phi}}\right), \qquad (2)$$

where $\omega = 2B_R M_T / B_T \Gamma$ is a fiber-dependent system constant and where the bleach rate could be deconvoluted into its thermal and optical contributions as $\varphi = \varphi_q + \varphi_P$. More precisely, these contributions are dependent on the fiber temperature and the intensity of the bleaching light as follows:

$$\varphi_{\mathrm{q}} = \varphi_{\mathrm{q0}} \exp\left(-\frac{E_{\mathrm{q}}}{\mathrm{k_B}T}\right), \qquad \varphi_{\mathrm{P}} = \frac{P\theta}{\sigma E_{\mathrm{P}}}, \qquad (3)$$

where φ_{q0} is the thermal escape frequency of the trap, E_q is the thermal activation energy of the trap, k_B is the Boltzmann constant, T is the temperature, P is the power of the bleaching light, θ is the photoionisation cross section of the trap at the wavelength of the photobleaching light, σ is the stimulation area, and E_P is the energy of the photobleaching light. Combining (2) and (3) yields an expression for $RIA_{sat}(P, T, \Phi)$, with associated system constants, as follows:

$$RIA_{\mathrm{sat}} = \frac{2RIA_{\mathrm{T}}}{\left(1 + \sqrt{1 + 2\omega\frac{\varphi_{\mathrm{q0}}}{\Phi}\exp\left(-\frac{E_{\mathrm{q}}}{\mathrm{k_B}T}\right) + 2\omega\frac{P\theta}{\sigma E_{\mathrm{P}}\Phi}}\right)}. \qquad (4)$$

We tested (4) against the data obtained from Experiments 1 and 2, physically constraining fits when reasonable. In all cases we assumed that $RIA_{end} \approx RIA_{sat}$, i.e., that the RIA_{end} values were representative of the saturation RIA values, unless otherwise noted. Again, this approximation holds only when

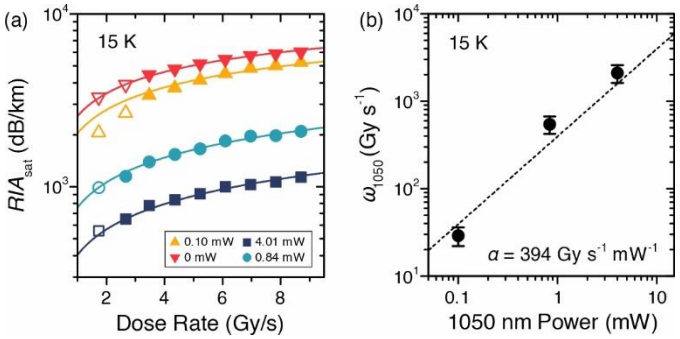

Fig. 5. (a) RIA_{sat} versus the dose rate for fibers 1 – 4 in Experiment 1 with different 1050 nm photobleaching powers. Symbols are the experimental RIA_{end} values and lines are fits to (5). Hollow symbols were excluded from the fit. (b) Fitted ω_{1050} values (symbols) against the measured power of the 1050 nm photobleaching light. The dashed line is a linear fit to the data.

$RIA(D)$ does not change significantly with dose. Moreover, the saturation RIA values should not significantly depend on dose history. This can be immediately tested by comparing the $RIA_{end}(\Phi, \varphi, T)$ values obtained from Experiments 1 and 2 for nearly equivalent (Φ, φ, T). Even though the fibers experienced dissimilar dose histories (i.e., a dose rate sweep for Experiment 1 and a temperature sweep for Experiment 2, and different cumulative doses), the measured RIA_{end}(8.7 Gy s^{-1}, φ, 15 K) values were approximately equivalent (within 5%) for similar φ across the two experiments.

It should also be noted that the model from which (4) is derived does not explicitly account for thermal effects unrelated to radiation. It is expected that the transmission, and therefore photobleaching efficacy, of both the 1550 nm and 1050 nm light will vary as a function of temperature, independent of radiation. These effects are neglected in our analysis. The model also assumes a broadly homogenous distribution of defects at different photobleaching powers and temperatures, which is a significant simplification of the problem [R1]. In Experiment 1, the temperature was very low and kept constant (T = 15 K), such that the thermal bleaching rate was presumed constant and small for all dose rates and photobleaching powers. The model predicts that, in the absence of any bleaching, $RIA_{sat} = RIA_T$ for all dose rates. As RIA_{sat} did in fact increase with dose rate when P_{1050} = 0 mW, this suggests that the approximately 2 mW of 1550 nm probe light in all fibers also contributes to photobleaching, which is expected [26], and/or that there remains some thermal contribution to bleaching even at 15 K. These contributions are presumed constant given the constant T and the approximately constant P_{1550} across all fibers. Separating and simplifying the constant and variable contributions, we obtain:

$$RIA_{\mathrm{sat}} = 2RIA_{\mathrm{T}} \Big/ \left(1 + \sqrt{1 + \frac{2\omega_{\mathrm{r}}}{\Phi} + \frac{2\omega_{1050}}{\Phi}}\right), \qquad (5)$$

where $\omega_r = \omega_q + \omega_{1550} = \omega(\varphi_q + \varphi_{1550})$, where φ_{1550} is the photobleaching contribution of the (constant) 1550 nm probe light, and $\omega_{1050} = \omega\varphi_{1050}$, where φ_{1050} is the photobleaching contribution of the (variable) 1050 nm photobleaching light.

The RIA_{sat} versus Φ for different P_{1050} were fit to (5), where RIA_T and ω_r were constants shared across all fibers, and ω_{1050} was allowed to vary due to the variations in P_{1050}, except for the fixed case $\omega_{1050} = 0$ for the $P_{1050} = 0$ mW fiber. All $\Phi = 1.74$ Gy s^{-1} data, and the $\Phi = 2.66$ Gy s^{-1} data for $P_{1050} = 0$ mW and 0.10 mW, were excluded from the fits as the RIA_{end} values were not ideal representations of the RIA_{sat} values (as $RIA(D)$ was still increasing significantly). The data and fits are shown in Fig. 5a and the fitted parameters are given in Table II.

TABLE II
PARAMETERS EXTRACTED FROM EXPERIMENT 1

Fiber	RIA_T (dB/km)	ω_r (Gy s^{-1})	ω_{1050} (Gy s^{-1})	P_{1050} (mW)
1	13422 ± 1425	44 ± 13	2105 ± 482	4.01
2			546 ± 125	0.84
3			29 ± 7	0.10
4			0	0

The fits were of good quality, demonstrating that the functional form of (5) describes the data well. The extracted RIA_T is in good agreement with data obtained for similar fibers, irradiated at similar temperatures, though with reduced 1550 nm probe intensities [19]. This implies that the residual bleaching component, ω_r, is mostly due to photobleaching by the probe light, which is expected for very low T. As $\omega_r \approx \omega_{1550}$, and ω is constant, we can compare ω_r and ω_{1050} to establish the relative photobleaching effectiveness, in terms of the photobleaching rates, of the 1550 nm and 1050 nm sources. Notably, ω_r and ω_{1050}(0.1 mW) are similar, implying that ~2 mW of 1550 nm light contributed to the sum photobleaching rate equivalent to approximately 0.1 mW of 1050 nm light. Thus, the 1050 nm light is approximately 20 times more effective at photobleaching the RIA at low temperatures than the 1550 nm light.

If the model is physically just, we expect the fitted ω_{1050} to vary linearly with the measured power of the 1050 nm photobleaching light per (3). An imperfect but generally linear relationship is in fact observed (Fig. 5b) with a constant of proportionality $\alpha = 394 \pm 100$ Gy s^{-1} mW^{-1}. Importantly, the model employed herein does not account for attenuation of the photobleaching light along the fiber length. For example, if we assume that the RIA at 1050 nm is similar to that at 1550 nm, then the 0.10 mW of photobleaching light will be attenuated by approximately 10 dB (to 0.01 mW) along the 2 m fiber at the end of the experiment. Conversely, the 4.01 mW of photobleaching light will be attenuated by approximately 2.3 dB (to 3.8 mW) along the 2 m fiber. Realistically, the RIA at 1050 nm will be several times that at 1550 nm, exacerbating this effect [24]. Thus, the photobleaching rate is a local parameter depending on the length of the fiber; moreover, RIA(D) is also localized. While experiments can be designed that test this phenomenon [30], conventional experiments measure the integrated RIA along the entire length of fiber. Thus, we measure an *effective* photobleaching rate for a 2 m length of fiber, and we should expect that smaller

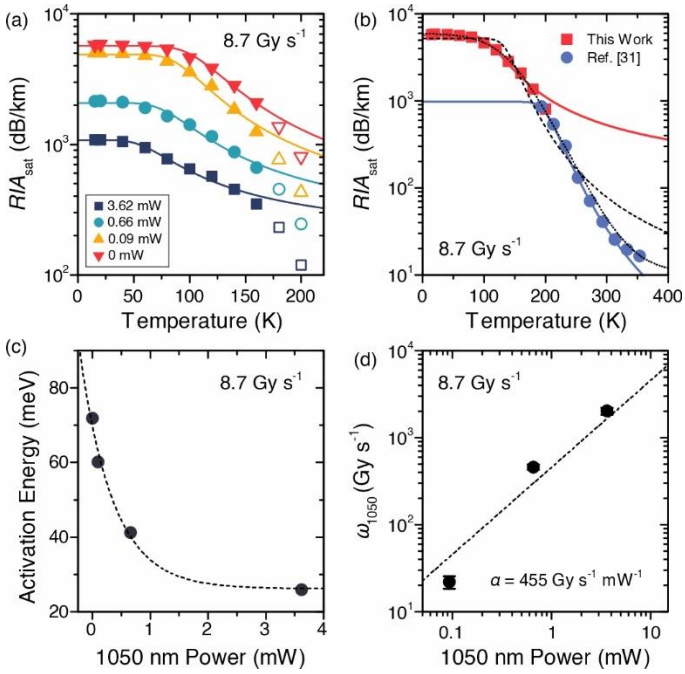

Fig. 6. (a) RIA_{sat} versus the temperature for fibers 1 – 4 in Experiment 2 with different 1050 nm photobleaching powers. Symbols are the experimental RIA_{end} values and lines are fits to (6). Hollow symbols were excluded from the fit. (b) Experimental RIA_{sat} data (symbols) and fits (lines) for $P_{1050} = 0$ mW and appended experimental RIA_{sat} data at higher temperatures extracted from [31] and the associated fit from [27]. The dashed line is a fit of all data to a variation on (6). (c) Fitted E_q values (symbols) against the measured power of the 1050 nm photobleaching light. The dashed line is an exponential decay fit to the data. (d) Fitted ω_{1050} values (symbols) against the measured power of the 1050 nm photobleaching light. The dashed line is a linear fit to the data.

photobleaching powers will be more significantly affected by the attenuation, leading to smaller relative ω_{1050} values. It is unsurprising then that the relationship between ω_{1050} and P_{1050} is not perfectly linear. This same effect explains why the lowest dose rate data points for the 0.1 mW RIA (Fig. 5a) deviate most significantly from the fit. As the bleaching light is attenuated, the growth rate of the RIA is affected, as $RIA(D)$ tends toward a length-dependent equilibrium. Using RIA_{end} to approximate RIA_{sat} during this period is not viable. A forthcoming work will focus on the effect of attenuated photobleaching light on RIA in greater detail. We note that the development of such a model has been initiated in the context of fiber dosimeters [R3].

In Experiment 2, the dose rate was high and kept constant (Φ = 8.7 Gy s^{-1}) while the irradiation temperature was decreased from 200 K to 15 K. From the previous analysis, we presumed that thermal bleaching at 15 K was negligible. Assuming the bleach rate from the 1550 nm probe light is temperature independent, we expect the same ω_{1550} for this experiment. As RIA_T is intrinsic to the fiber type, we similarly expect the same RIA_T. The measured 1050 nm powers were similar to, though distinct from, those in Experiment 1 due to coupling losses, so we expect slightly different 1050 nm photobleaching rates. As the temperature was varied, we must

use the full variable form of φ_q. Separating and simplifying the constant and variable contributions, we obtain:

$$RIA_{sat} = 2RIA_T \Big/ \left(1 + \sqrt{1 + \frac{2(\omega_{1550} + \omega_{1050})}{\Phi} + \frac{2\omega_{q0} \exp\left(-\frac{E_q}{k_B T}\right)}{\Phi}} \right), \quad (6)$$

where $\omega_{q0} = \omega\varphi_{q0}$.

The RIA_{sat} versus T for different P_{1050} are shown in Fig. 6a. A cursory inspection of the data reveals that there are multiple kinetic components at play, particularly for higher photobleaching powers, for which multiple inflection points were observed. We therefore limited our focus to a temperature range for which a single kinetic component was a good approximation, which was $T \leq 160$ K. These RIA_{sat} data were fit to (6), where RIA_T and ω_{q0} were constants shared across all fibers, $\omega_{1550} = 44$ Gy s^{-1} for all fibers, $\Phi = 8.7$ Gy s^{-1} for all fibers, ω_{1050} was allowed to vary due to the variations in P_{1050}, except for the fixed case $\omega_{1050} = 0$ for the $P_{1050} = 0$ mW fiber, and E_q was also allowed to vary. Initially, we attempted fitting using a shared E_q value, though the fits were poor. Only data up to $T \leq 160$ K were included in the fits. The fits are also shown in Fig. 6a, and the fitted parameters are given in Table III.

TABLE III
PARAMETERS EXTRACTED FROM EXPERIMENT 2

Fiber	RIA_T (dB/km)	ω_{q0} (Gy s^{-1})	ω_{1050} (Gy s^{-1})	E_q (eV)	P_{1050} (mW)
1	12280 ± 172	86887 ± 20424	2024 ± 185	0.026 ± 0.002	3.62
2			461 ± 33	0.041 ± 0.003	0.66
3			22 ± 4	0.069 ± 0.003	0.09
4			0	0.072 ± 0.003	0

The fits were of decent quality over the defined range of temperatures, demonstrating that the functional form of (6) describes the data well under certain conditions. Clearly, the fits fail to describe the RIA_{sat} at temperatures >160 K. As discussed in our earlier work [27], the model applied herein is derived for a single defect with a single set of defining parameters. However, it is well known that different defects dominantly contribute to RIA at different temperatures [24]. Assuming at least two defects contribute to RIA over the tested temperature range, each will be characterized by a distinct set of parameters, e.g., frequency factors and activation energies. If these parameters are dissimilar, the model will fail to capture the properties of both defects. Therefore, it is likely that a single defect that can be described using the parameters in Table III dominates the RIA of the fibers studied herein below approximately 160 K, and a distinct defect with distinct parameters dominates the RIA at higher temperatures.

To test this hypothesis, we appended data extracted from [31], also pertaining to SMF28e+ fiber, to those presented in this work for $P_{1050} = 0$ mW (Fig. 6b). Despite the experiments being performed using different equipment, and at different dose rates with different 1550 nm probe powers, the data are in good agreement at 200 K and RIA_{sat} continues to decrease smoothly up to over 350 K. The data in [31] were earlier tested against a variation of (6), from which the parameters $RIA_T = 974$ dB/km, $\omega_{q0} = 3.4 \times 10^9$ Gy s^{-1}, and $E_q = 0.39$ eV were extracted. Clearly, the properties of the defects contributing to RIA over the wider temperature range vary significantly. Convoluting these defects by supposing that the data over the entire range (i.e., 15 K to 350 K) could be described using a single representative defect, we fit the entire range of data to a variation of (6), shown in Fig. 6b. The fit was generally quite poor, and the significant extracted parameters were then $RIA_T = 5187$ dB/km and $E_q = 0.19$ eV, corresponding to intermediate values relative to those obtained from the distinct temperature ranges. To properly deconvolute the properties of the individual defects, it should be possible to make spectrally resolved RIA measurements over the entire temperature range [24]. This will be attempted in future works.

We also tested the ability of a simple sigmoidal (Boltzmann) function to describe the data (Fig. 6b), per the empirical approach employed in [R3]. The fit was good over the entire temperature range 15 K to 350 K, despite the expected dominance of different defects at different temperatures [24]. This indicates that empirically-derived models may provide improved predictive power over the physically-derived model tested in this work, under particular experimental conditions.

As mentioned earlier, sharing E_q across the fibers with different P_{1050} produced poor fits, which was remedied by allowing E_q to vary as a function of P_{1050}. This requirement is not surprising, given that the model presumes that the RIA active defect is characterized by a single thermal trap depth, while real world systems (in particular, amorphous materials such as glasses) generally contain defects with a distribution of trap depths [32], [33], [34]. In fact, the effective E_q likely varies slightly as a function of temperature, as shallower (i.e., smaller E_q) traps in the distribution are emptied first at lower temperatures. Regardless, the E_q values extracted from the fits decreased exponentially as P_{1050} increased (Fig. 6c), signifying a strong correlation between thermal activation energy and photobleaching rate. This effect may be due to physical coupling between the optical and thermal bleaching phenomena (e.g., a form of photothermal ionization), or alternatively the measured E_q may be smaller for larger P_{1050} due to reduced defect concentrations and/or different trapping/detrapping rates across the distribution of E_q. In either case, it appears that photobleaching enhances thermal bleaching in certain temperature ranges, aiding to further suppress the RIA.

TABLE IV
SMF28E+ MODEL PARAMETERS

RIA_T (dB/km)	12280	E_{q0} (eV)	0.026
ω_{1550} (Gy s^{-1})	44	A_q (eV)	0.043
ω_{q0} (Gy s^{-1})	86887	k_q (mW^{-1})	1.73
α (Gy s^{-1} mW^{-1})	424.5		

Otherwise, the RIA_T obtained for Experiment 2 is the same as that obtained for Experiment 1, within uncertainty. Again, an imperfect but generally linear relationship is observed between the fitted ω_{1050} values and P_{1050} (Fig. 6d) with a constant of proportionality $\alpha = 455 \pm 143$ Gy s^{-1} mW^{-1}, which is the same as that obtained for Experiment 1, within uncertainty. Consequently, it should be possible to use a single set of parameters, characteristic of SMF28e+ fibers, to calculate RIA_{sat} under all experimental conditions for which those parameters are representative of the primary defect producing RIA, using only the experimental conditions as inputs (i.e., dose rate, 1050 nm power, and temperature). To that end, we used the parameters given in Table IV, derived from the fits, to calculate, using (7), RIA_{sat} values for all conditions across both experiments.

$$RIA_{sat} = 2RIA_T \Big/ \left(1 + \sqrt{1 + \frac{2(\omega_{1550} + \alpha P_{1050})}{\Phi} + \frac{2\omega_{q0}\exp[-(E_{q0} + A_q \exp[-k_q P_{1050}])/k_B T]}{\Phi}}\right). \quad (7)$$

The calculated and experimental RIA_{sat} values are plotted against one another in Fig. 7. Neglecting the $T > 160$ K data (hollow symbols), the calculated and experimental values are in good agreement over an order of magnitude, and from 15 K to 160 K, P_{1050} from 0 mW to approximately 4 mW, and Φ from 1.74 Gy s^{-1} to 8.7 Gy s^{-1}. Excluding the T >160 K data, all values (N = 72) are within ±30%, and most of the values (N = 47) are within ±10%, of the experimental data. Thus, despite the many approximations and physical limitations of the OTOR-derived RIA saturation model, it appears that a single set of parameters can be used to approximate experimental RIA_{sat} values with decent accuracy, over a wide range of experimental conditions.

V. CONCLUSION

We studied the combined effects of radiation dose rate, irradiation temperature, and secondary photobleaching power on the RIA of standard germanosilicate optical fibers (Corning SMF28e+). The dose rates varied from approximately 1.7 Gy s^{-1} to 8.7 Gy s^{-1}, the temperature varied from 15 K to 200 K, and the secondary photobleaching power at 1050 nm varied from 0 mW to approximately 4 mW. Fibers were irradiated up to high cumulative doses exceeding 1 MGy and the RIA was monitored at 1550 nm throughout each experiment. We focused our analyses on the high dose RIA (i.e., the saturation RIA_{sat}) values. We found that RIA_{sat} increased as the dose rate increased, decreased as the temperature increased, and decreased as the photobleaching power increased. The interdependence of these conditions was further analyzed

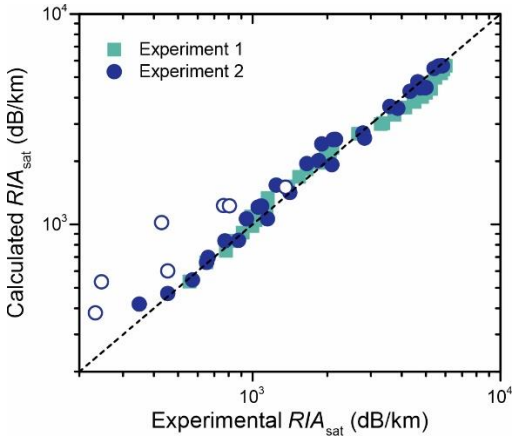

Fig. 7. Calculated RIA_{sat} using the parameters in Table IV with (7) versus the experimental RIA_{sat} values from Experiments 1 & 2. Hollow symbols are data from Experiment 2 where $T > 160$ K. The dashed line represents perfect agreement between the calculated and experimental values.

using a recently developed model [27]. The model successfully quantitatively captured the behavior of RIA_{sat} as a function of dose rate, irradiation temperatures at and below 160 K, and photobleaching power, and enabled the extraction of fiber-specific parameters useful for further calculations. Ultimately, we demonstrated that a single set of fixed parameters could be used to calculate RIA_{sat} as a function of the experimental inputs with reasonable accuracy.

REFERENCES

[1] Y. Deng and J. Jiang, "Optical fiber Sensors in extreme temperature and radiation environments: A review", *IEEE Sensors Journal*, vol. 22, no. 14, pp. 13811-13834, July 2022.

[2] W. Ecke, I. Latka, R. Willsch, A. Reutlinger, R. Graue, "Fibre optic sensor network for spacecraft health monitoring", *Meas. Sci. Tech.*, vol. 12, no. 7, pp. 974-980, July 2001.

[3] A. Rovera, A. Tancau, N. Boetti, M.D.L. Dalla Vedova, P. Maggiore, D. Janner, "Fiber optic sensors for harsh and high radiation environments in aerospace applications, *Sensors*, vol. 23, no. 5, Art. no. 2512, March 2023.

[4] P.F. Kashaykin *et al*., "Radiation resistance of single-mode optical fibers with view to in-reactor applications", *Nuclear Materials and Energy*, vol. 27, Art. no. 100981, June 2021.

[5] P. Paillet *et al*., "Phosphosilicate Multimode Optical Fiber for Sensing and Diagnostics at Inertial Confinement Fusion Facilities", *IEEE Sensors Journal*, vol. 22, no. 3, pp. 22700-22706, Dec. 2022.

[6] J. Blanc *et al*., "Characterization of radiation-resistant multimode optical fibers for large-scale procurement", *IEEE Trans. Nucl. Sci.* vol. 68, no. 7, pp. 1407-1413, July 2021.

[7] T. Wijnands, L.K. De Jonge, J. Kuhnhenn, S.K. Hoeffgen, U. Weinand, "Optical absorption in commercial single mode optical fibers in a high energy physics radiation field", *IEEE Trans. Nucl. Sci*., vol. 55, no. 4, pp. 2216-2222, Aug. 2008.

[8] D.C. Van Der Laan, J.D. Weiss, F. Scurti, J. Schwartz, "CORC® wires containing integrated optical fibers for temperature and strain monitoring and voltage wires for reliable quench detection", *Supercond. Sci. Technol.*, vol. 33, no. 8, Art. no. 085010, Aug. 2020.

[9] C. Balbier, S. Bucks, F. Scurti, S. Lee, "High-temperature fiber optic sensor performance for heat pipe instrumentation", *IEEE Sensors Journal*, vol. 25, no. 10, pp.17117-17127, May 2025.

[10] C. Karapanagiotis, M. Schukar, K. Krebber, "Distributed fiber optic sensors for structural health monitoring of composite pressure vessels", *Technisches Messen* vol. 91, no. 3-4, pp. 168-179, April 2024.

[11] S. Girard *et al*., "Overview of radiation effects on silica-based optical fibers and fiber sensors", *IEEE Trans. Nucl. Sci.*, vol. 72, no. 4, pp. 982-1020, April 2025.

[12] F.S. Fernandez *et al*., "Photobleaching of neutron radiation induced attenuation of optical fibers at liquid nitrogen temperature", *IEEE Trans. Nucl. Sci*., vol. 72, no. 7, pp. 2145-2153, July 2025.

[13] M. Roche *et al*., "Temperature dependence of the radiation response of ultralow-loss optical fibers: role of self-trapped holes", *IEEE Trans. Nucl. Sci*., vol. 72, no. 4, pp. 1165-1171, April 2025.

[14] I. Toccafondo *et al*., "Irradiation of multimode Ge-doped and F-doped optical fibers at cryogenic temperatures down to 10 K", *Journal of Lightwave Technology*, vol. 41, no. 1, pp. 286-292, Jan. 2023.

[15] R. Pecorella *et al*., "Influence of manufacturing parameters on the steady state radiation response of radiation sensitive optical fibers", *IEEE Trans. Nucl. Sci*., vol. 72, no. 8, pp. 2555-2561, Aug. 2025.

[16] P.F. Kashaykin, E.A. Pospelova, Y.O. Sharonova, O.L. Vokhmyanina, I.S. Azanova, A.L. Tomashuk, "Temperature and polarization dependence of radiation-induced attenuation in pure-silica-core PANDA optical fiber", *Optical Materials*, vol. 131, Art. no. 112510, Sep. 2022.

[17] C. Campanella *et al*., Temperature dependence of radiation induced attenuation of aluminosilicate optical fiber, *IEEE Trans. Nucl. Sci*. vol. 69, no. 7, pp. 1515-1520, July 2022.

[18] J. Blanc, D. Ricci, J. Kuhnhenn, U. Weinand, O.J. Schumann, "Irradiation of radiation-tolerant single-mode optical fibers at cryogenic temperature", *Journal of Lightwave Technology*, vol. 35, no. 10, pp. 1929-1935, May 2017.

[19] J. Kuhnhenn, O.J. Schumann, U. Weinand, R. Wolf, "Gamma irradiation test of Ge-doped single-mode optical fiber at cryogenic conditions", *2016 RADECS*, Bremen, Germany, 2016, pp. 1-4.

[20] S. Zilberman *et al*., "Near infrared radiation induced attenuation in P-doped and Al-doped optical fibers at cryogenic temperature", *Optics Continuum*, vol. 4, no. 7, pp. 1411-1425, July 2025.

[21] F. Solis Fernandez *et al*., "Mitigation of radiation-induced attenuation of optical fibers through photobleaching: study of power dependence at cryogenic temperatures", *Proc. SPIE 12929, Sensors and Smart Structures Technologies for Civil, Mechanical, and Aerospace Systems*, Art. no. 129490A, May 2024.

[22] F. Solis Fernandez *et al*., "Mitigation of high X-ray dose radiation-induced attenuation in optical fibers at 15 K: effect of cumulative dose", *Optical Engineering*, vol. 64, no. 7, Art. no. 076101, July 2025.

[23] M. Roche *et al*., "Combined photobleaching and temperature effects on 1550 nm radiation-induced attenuation of germanosilicate optical fiber, *IEEE Trans. Nucl. Sci.*, vol. 70, no. 8, pp. 1951-1957, Aug. 2023.

[24] A. Morana *et al*., "Photobleaching effects on the radiation-induced attenuation of germanosilicate optical fibers at low temperature", *IEEE Trans. Nucl. Sci*., vol. 72, no. 8, pp. 2548-2554, Aug. 2025.

[25] J.J. Schuyt, O. Duke, D.A. Moseley, B.M. Ludbrook, E.E. Salazar, R.A. Badcock, "Gamma irradiation of Ge-doped and radiation-hard silica fibers at cryogenic temperatures: Mitigating the radiation-induced attenuation with 1550 and 970 nm photobleaching", *J. Appl. Phys.*, vol. 134, no. 4, Art. no. 043103, July 2023.

[26] C. Campanella *et al*., "Photobleaching effect on infrared radiation-induced attenuation of germanosilicate optical fibers at MGy dose levels", *IEEE Trans. Nucl. Sci*., vol. 68, no. 8, pp. 1688-1693, Aug. 2021.

[27] J.J. Schuyt, D.A. Moseley, B.M. Ludbrook, S.M. Haneef, R.A. Badcock, "Modeling the radiation-induced attenuation limits in optical fibers during concurrent irradiation, thermal annealing, and photobleaching", *IEEE Trans. Nucl. Sci.*, vol. 72, no. 7, pp. 2154-2162, July 2025.

[28] D.L. Griscom, "Fractal kinetics of radiation-induced point-defect formation and decay in amorphous insulators: Application to color centers in silica-based optical fibers", *Phys. Rev. B*, vol. 64, no. 17, Art. no. 174201, Oct. 2001.

[29] D.L. Griscom, "γ-Ray-induced visible/infrared optical absorption bands in pure and F-doped silica-core fibers: Are they due to self-trapped holes?", *J. Non. Cryst. Solids*, vol. 349, pp. 139-147, Dec. 2004.

[30] O. Duke, J. Desroches, E. Salazar, "Length-resolved measurement of radiation induced attenuation in quench detection optical fibers with photobleaching", *IEEE Transactions on Applied Superconductivity*, vol. 35, no. 5, Art. no. 9500504, Aug. 2025.

[31] A. Morana *et al*., "Temperature dependence of low-dose radiation-induced attenuation of Germanium-doped optical fiber at infrared wavelengths", *IEEE Trans. Nucl. Sci.*, vol. 69, no. 3, pp. 512-517, March 2022.

[32] D.L. Griscom, "Self-trapped holes in pure-silica glass: A history of their discovery and characterization and an example of their critical significance to industry", *J. Non. Cryst. Solids*, vol. 352, no. 23-25, pp. 2601-2617, July 2006.

[33] P. V. Sushko, S. Mukhopadhyay, A.S. Mysovsky, V.B. Sulimov, A. Taga, A.L. Shluger, "Structure and properties of defects in amorphous silica: New insights from embedded cluster calculations", *Journal of Physics Condensed Matter*, vol. 17, no. 21, Art. no. S2115, June 2005.

[34] F. Mady *et al*., "Optical fibers under irradiation: quantitative assessment of the energy distribution of radiation-induced trapped states", *Proc. SPIE 11357, Fiber Lasers and Glass Photonics*, Art. no. 113571B, April 2020.

[R1] M. Roche et al., "Temperature Cycling Effects on Infrared Radiation-Induced Attenuation of Silica-Based Optical Fibers", *IEEE Trans. Nucl. Sci*., vol. 71, no. 4, pp. 744-751, Apr. 2024.

[R2] S. Girard et al., "Overview of radiation induced point defects in silica-based optical fibers", *Reviews in Physics*, vol. 4, Art. no. 100032, Nov. 2019.

[R3] F. Fricano et al., "Photobleaching Effect on the Sensitivity Calibration at 638 nm of a Phosphorus-Doped Single-Mode Optical Fiber Dosimeter", *Sensors*, vol. 24, no. 17, Art. no. 5547, Aug. 2024.

[R4] J. Perrot et al., "Combined Radiation and Temperature Effects on Brillouin-Based Optical Fiber Sensors", *Sensors*, vol. 10, no. 12, Art. no. 1349, Dec. 2023.

[R5] S. Girard et al., "Combined High Dose and Temperature Radiation Effects on Multimode Silica-Based Optical Fibers", *IEEE Trans. Nucl. Sci.*, vol. 60, no. 6, pp. 4305-4313, Dec. 2013.